A seismological large-N multisensor experiment to study the magma transfer of intracontinental volcanic fields: The example of the Eifel, Germany

T. Dahm [ID] * [1,2], M. Isken [ID] [1], C. Milkereit [1], Ch. Sens-Schönfelder [ID] [1], F. Eckel [ID] [3], X. Yuan [ID] [1], M. C. Reiss [ID] [4,8], G. Petersen [ID] [1], S. Cesca [ID] [1], A. Oth [ID] [7], G. Rümpker [ID] [8], L. De Siena [ID] [4,10], P. Büyükakpinar [ID] [1], P. Laumann, [ID] [1], H. Zhang, [ID] [1], B. Knapmeyer-Endrun [ID] [11,12], S. Mikulla [1], R. Bauz [1], S. Busch [9], M. Hensch [ID] [5], B. Schmidt [6]

[1]GFZ Helmholtz Centre for Geosciences, Potsdam, Germany, [2]Institute of Geosciences, University of Potsdam, Potsdam, Germany, [3]Kiel University, Kiel, Germany, [4]Institute for Geosciences, Johannes Gutenberg University of Mainz, Mainz, Germany , [5]LEB Freiburg, Germany , [6]Geological-Survey Mainz, Germany , [7]European Center for Geodynamics and Seismology, Walferdange, Luxembourg , [8]Institute for Geosciences, Goethe University Frankfurt, Germany , [9]Geologischer Dienst NRW, Germany , [10]Dept. of Physics and Astronomy, University of Bologna, Italy , [11]Bensberg Observatory, University of Cologne, Cologne, Germany , [12]Now at: Microgravity User Support Center, German Aerospace Center (DLR), Cologne, Germany

Author contributions: *Conceptualization*: Torsten Dahm. *Pre-site survey*: CM. *Network design*: TD, MI, CSS, SS. *Station preparation*: SM, RB. *Field experiment contribution*: CM, MI, CSS, FE, XY, MCR, SC, AO, GR, PB, PL, BKE, SM, RB, MH, BS. *Methodology*: TD, MI, FE, XY, MCR, GP. *Software*: MI, FE, MCR, GP. *Formal Analysis*: MI, TD, FE, MCR, GP, HZ. *Data curation*: MI, CSS. *Writing - Original draft*: TD. *Writing - Review & Editing*: TD, CSS, FE, MCR, GP, GR, LDS, PB, XY, SC. *Visualization*: TD, MI, GP, FE, MCR, XY.

Abstract The understanding of the magma system beneath intracontinental volcanic fields depends critically on our ability to resolve small-sized anomalies distributed over large areas of hundreds of kilometres. Magmatic reservoirs co-exist at different depths in the upper mantle and crust and may consist of extensive zones of crystal mush, swarms of sills and dikes of different ages and states, pore space saturated by volatiles or melt, or larger-volume, differentiated magma. Passive seismological experiments with a large number of sensors deployed with small interstation spacings, combining different types of sensors and fibre-optic sensor technology, have great promise for addressing the resolution to capture the distributed magmatic system. We report on a one-year, large-N experiment in the Quaternary volcanic fields of the Eifel, Germany, where more than 494 seismic stations were deployed and combined with a 64 km long DAS cable and permanent stations. A cloud-based, open-source GIS system was implemented to address logistical challenges and ensure data quality combined with seismological analysis and visualisation tools. We present initial results to test the potential of such an extensive waveform database and automated processing for locating small earthquakes and imaging crustal and upper mantle anomalies using techniques such as ambient noise cross-correlation, receiver functions, and SKS splitting.

Zusammenfassung Verteilte Vulkanfelder sind eine wenig erforschte Form des Vulkanismus innerhalb kontinentaler Platten. Sie zeichnen sich durch eine große Anzahl von Vulkanen und Maaren aus, die sich über Gebiete von 1.000 bis 10.000 km² verteilen. In den meisten Fällen ist jeder dieser Vulkane nur einmal aktiv, die folgenden Eruptionen finden dann an einem anderen Ort statt. Um die Gefahr durch diese Art des Vulkanismus besser einschätzen zu können, ist es wichtig, das magmatische System von der Manteltiefe bis zur oberen Kruste abzubilden und kleine Magmakammern zu kartieren, aus denen Magmen aufsteigen und einen einzelnen Ausbruch verursachen könnten. Wir haben ein großes passives seismisches Experiment in den Vulkanfeldern der Eifel in Deutschland durchgeführt. Dabei setzten wir mehr als 494 seismische Stationen in Kombination mit Lichtleiter-Sensorik entlang eines ungenutzten, 64 Kilometer langen Telekommunikationskabels sowie permanenten Stationen in der Region ein. Der Übersichtsartikel beschreibt die wissenschaftliche Motivation, den Versuchsaufbau, die Datenqualität und das enorme Potenzial der umfangreichen Wellenformdatenbank. Wir zeigen, wie neuartige Techniken der künstlichen Intelligenz eingesetzt werden, um kleine Mikroerdbeben direkt aus den Wellenformen automatisch zu lokalisieren. Es werden Beispiele für die Abbildung von Anomalien in der Erdkruste und im oberen Mantel vorgestellt.

Non-technical summary Distributed volcanic fields are a poorly understood type of volcanism within continental plates. They are characterized by a large number of volcanoes and maars densely distributed over areas of 1000 to 10000 km^2. In most cases, each of these volcanoes are active only once in their life, and the following eruptions occur at a different location.

*Corresponding author: dahm@gfz.de

To better assess the hazard of this type of volcanism, it is important to image the magmatic system from the mantle depth to the upper crust and to map small magma pockets, where the magma is often stored and from where it could rise to form a single eruption. We conducted a large passive seismic experiment in the Eifel volcanic fields, Germany, using more than 494 seismic stations combined with acoustic sensing along an unused 64 km long telecommunication cable and permanent stations in the region. The overview paper describes the scientific motivation, the experimental setup and data quality, and the huge potential of the collected extensive waveform database. We show how novel artificial intelligence techniques are used to automatically locate small microearthquakes directly from the waveforms. Examples for imaging crustal and upper mantle anomalies are presented.

1   Introduction

Distributed volcanic fields are the most common form of continental volcanism away from plate boundaries. The magma dynamics and volcanic hazards of these fields remain largely undetermined because their volcanic centres do not exhibit any temporally predictable eruption patterns (e.g., Alohali et al., 2022). Moreover, their magmatic feeder systems are distributed over large depth ranges in the crust and mantle, and magma transfer ranges from rapid melt ascent of primitive magmas directly from the mantle to protracted development in intracrustal magma reservoirs.

The chain of volcanic fields from northern Spain, France and Germany, including the Eifel (Fig. 1), is a world-class example of young distributed volcanism in central Europe. The Eifel is notable not only for the size of its two Quaternary subfields, the Eastern Eifel Volcanic Field (EEVF) and the Western Eifel Volcanic Field (WEVF), each about 60 x 40 km^2 (Fig. 1a), but also for its eruption rate, with more than 350 eruptions within about 700 ka (Fig. 1b). Between the two Quaternary fields lies a Tertiary volcanic field in the High Eifel. The numerous volcanoes show a wide range of eruption types, from small scoria cones and explosive maar-diatreme volcanoes to long-lived volcanic centers in the EEVF, that produced highly explosive, large-volume eruptions of evolved, gas-rich magma. All known eruptions in the Eifel occurred at prehistoric times in a now highly urbanized region.

Laacher See volcano (LSV, Fig. 1a) features an actively degassing, CO_2-rich magma system. High background CO_2-fluxes, ephemeral gas bursts, and CO_2-driven diatremes go along with short-term uplift and deflation, indicating a highly active yet cold hydrothermal system. Why this system appears cold on the surface is enigmatic in the light of the size of a Volcanic Explosivity Index 6 eruption (VEI 6) only 13 ka ago (Reinig and et al., 2021). Laacher See is also unique as the second youngest silicate-carbonatitic magma system worldwide that is not erupting. CO_2 from mantle melts and evolved phonolitic magma chambers strongly influence magma properties and the surrounding country rock. With more than 200 springs with $CO_2 > 1\,g/l$ and a CO_2 flux of about $5\,kt/a$ only at LSV (e.g., Dahm et al., 2020), the Eifel region is a world-class location to study the role of magmatic CO_2 as a potential hazard and indicator for fluid transport from the mantle to the surface.

Besides LSV, there are older phonolitic volcanoes in the EEVF: the Wehr ($\sim 150\,ka$) and Rieden complexes ($\sim 450\,ka$) few kilometers west and southwest of LSV

(Fig. 1). Evolved alkaline volcanism in these centers, including LSV, is associated with ejection of cogenetic carbonatite clasts, which were segregated from underground carbonatite intrusions (Schmitt et al., 2010; Berndt and Klemme, 2022).

Degassing from stalled magma at Moho depths with ongoing migration of magmatic fluids through the crust beneath the EEFZ is likely related to the occurrence of deep low-frequency (DLF) earthquakes in persistent depth clusters (Hensch et al., 2019). The first DLF earthquakes were detected in 2013, and since then, several deep clusters have been active, indicating a transcrustal subvertical channel structure between 10 and 45 km depth, which is likely used by CO_2-rich fluid and/or melt to migrate upwards. This transcrustal channel coincides with the location where the highest CO_2 flux and highest ratios of helium isotopes ($Ra = {}^3He/{}^4He$ corrected for atmospheric contamination) were measured with $Ra = 5.6$ in the region between Wehr and the LSV.

Geochemical and petrological studies constrain the uppermost level of the transcrustal magma system in the EEVF to 3–4 km (115–145 MPa pressure, Berndt et al., 2001), consistent with depth estimates for phonolitic magma reservoirs at 4–12 km from erupted contact metamorphic xenoliths. The analysis of tephra from the LSV VEI 6 eruption indicates that an interconnected, thermally and compositionally stratified phonolitic magma reservoir existed before eruption (e.g. Tomlinson et al., 2020, and references therein). Detailed studies of diffusion modelling of zoned feldspar revealed that the intrusive complex remained hot ($> 560°C$, Rout and Wörner, 2018, 2020) over several tens of thousands of years preceding the eruption (Bourdon et al., 1994; Schmitt et al., 2010). This requires frequent influx of fresh magma to keep the system hot.

Mantle-derived CO_2 also plays an important role in controlling crystal-melt stability in magma reservoirs, and flushing of crystal-rich mush reservoirs by arrival of large amounts of ascending CO_2 has been proposed as an eruption trigger (Caricchi et al., 2018; Pappalardo et al., 2022). Since swarm-like microearthquakes have occurred in 2017/2018 and 2022 between and below all three centers at a depth of about 8 km, it is postulated that a common sill-like reservoir remains active underneath. An example of the geometry of a sill or saucer-type reservoir is given in the West Eifel beneath Kelberg (see, Dahm et al., 2020), where seismic profiling resolved a 10 km wide bright spot between 6 and 10 km depth, which correlates with a circular magnetic and gravity anomaly and is interpreted as the remnant of a tertiary magma reservoir.
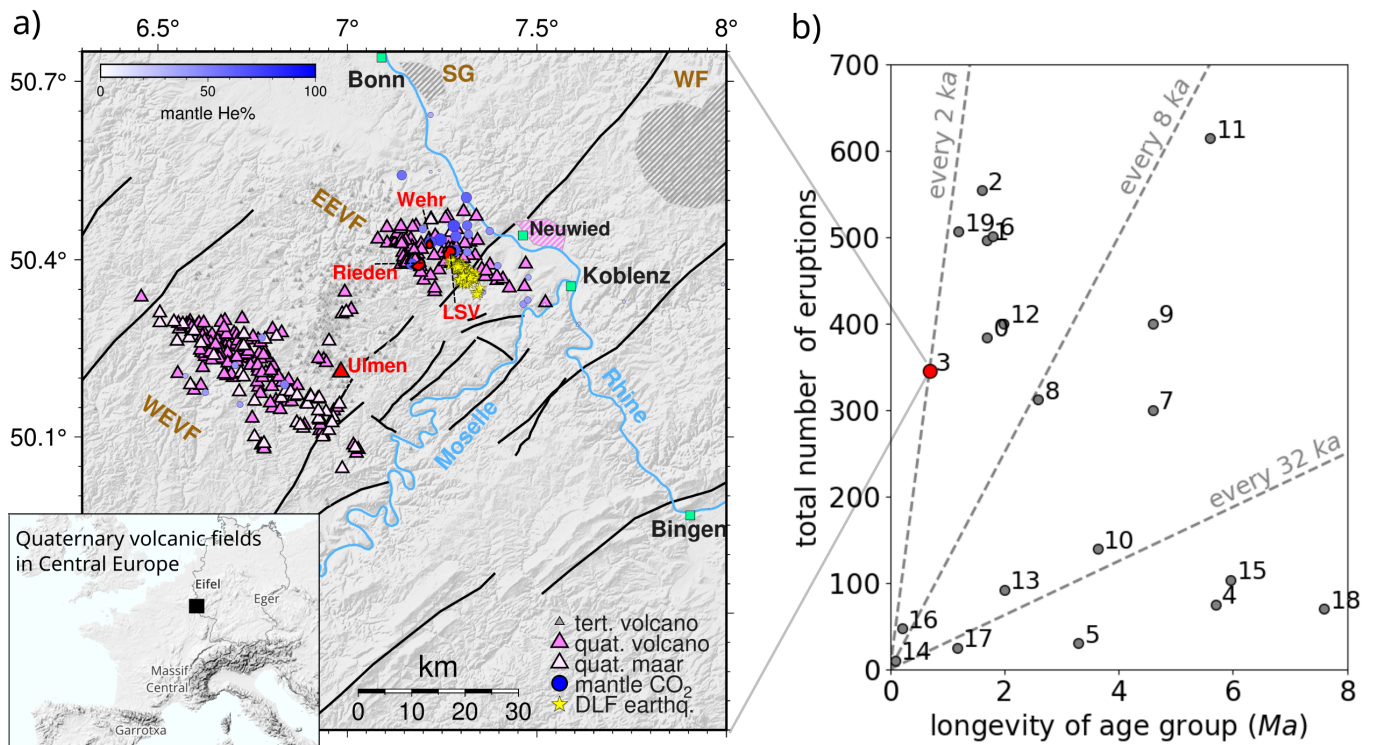
Figure 1 (a) Overview of the Quaternary (EEVF, WEVF) and Tertiary volcanic fields in the Eifel. The hatched areas show the Tertiary fields of the Siebengebirge (SG) and Westerwald (WF). Small gray triangles indicate tertiary volcanoes of the high Eifel. Rieden, Wehr and Laacher See (LSV) are phonolitic eruption centers, where the youngest explosive eruption occurred 13 ka ago at LSV. The youngest maar eruption occurred 11 ka ago at Ulmen. Emission points for magma-derived CO_2 with mantle-derived helium (He, blue circles) and major faults (black lines) are shown. The inlet figure shows the Eifel region (black box) and provides an overview of Quaternary volcanic fields in Central Europe. (b) Global assessment of recurrence time of intracontinental volcanic fields, where the Eifel Quaternary fields are highighted in red. Label numbers refer to: 0=Harrat Khaybar; 1=Northern Harrat Rahat; 2=Armenia; 3=Eifel Quaternary Volcanic Fields, Germany; 4=Pancake, USA; 5=Yucca Mountain, USA; 6=Springerville, USA; 7=Camargo, Mexico; 8=Klyuchevskoy Group, Russia; 9=Newer VP, Australia; 10=Pali Aike, Argentina; 11=San Francisco, USA; 12=Pinacate, Mexico; 13=Coso, USA; 14=Hurricane, USA; 15=Lunar Crater, USA;16=Sabatini, Italy; 17=Big Pine, USA; 18=Cima, USA; 19=Eastern Snake River Plain, USA (compilation from Alohali et al., 2022).

Recent geophysical and geodetical observations have also challenged preconceptions about the deep structure of the Eifel volcanic field. For instance, ongoing regional-scale uplift of the Rhenish massif (e.g., Kreemer et al., 2020) is identified in GNSS and PSInSAR ten- or twenty-year average velocities. Interestingly, the surface uplift rate correlates with the intensity of the Moho velocity anomaly and the smooth Moho upwelling over distances of more than 100 km (Fig. S3 in supplement material). The uplift rate also peaks where Moho upwelling is indicated in a seismic profile through the Eifel along with a lower crustal seismically transparent wedge in the lower crust (see Dahm et al., 2020, and supplement material).

Starting in September 2022, we conducted a year-long large-N seismological experiment in the Eifel region with more than 494 seismic station locations and an outstanding dense ray coverage with about 80,000 theoretical pathways for seismic waves (Fig. 2). The seismic stations consisted of 4.5 Hz short period geophones, Mark 1 Hz and Trillium compact broadband sensors (20 s & 120 s). The interstation distance of the distributed array is about 1 km in the EEVF and close to the Laacher See. Additionally, three small aperture arrays were deployed in a tripartite configuration (6-8 stations within 200 m), surrounding the Laacher See, recording at 200 Hz. In spring 2023, the network was partly re-distributed to realise a 180 km long linear profile crossing the LSV with an interstation distance of only 1 km (Fig. 2). The stations recorded data over a period of one year and all data were collected end of August 2023. Additionally, for the first time in Germany, we interrogated a 64 km long, unusued telecomunications cable (dark fibre) running through the study area (Fig. 4) to continuously monitor strain rates on 5500 virtual channels at a sampling rate of 250 Hz (Distributed Acoustic Sensing, DAS). As a further activity, a first shallow scientific borehole was realized in a joint effort of the Geological Survey of Rhineland-Palatinate and the GFZ, which was equipped with a borehole seismometer at a depth of 225 m depth to improve the monitoring.
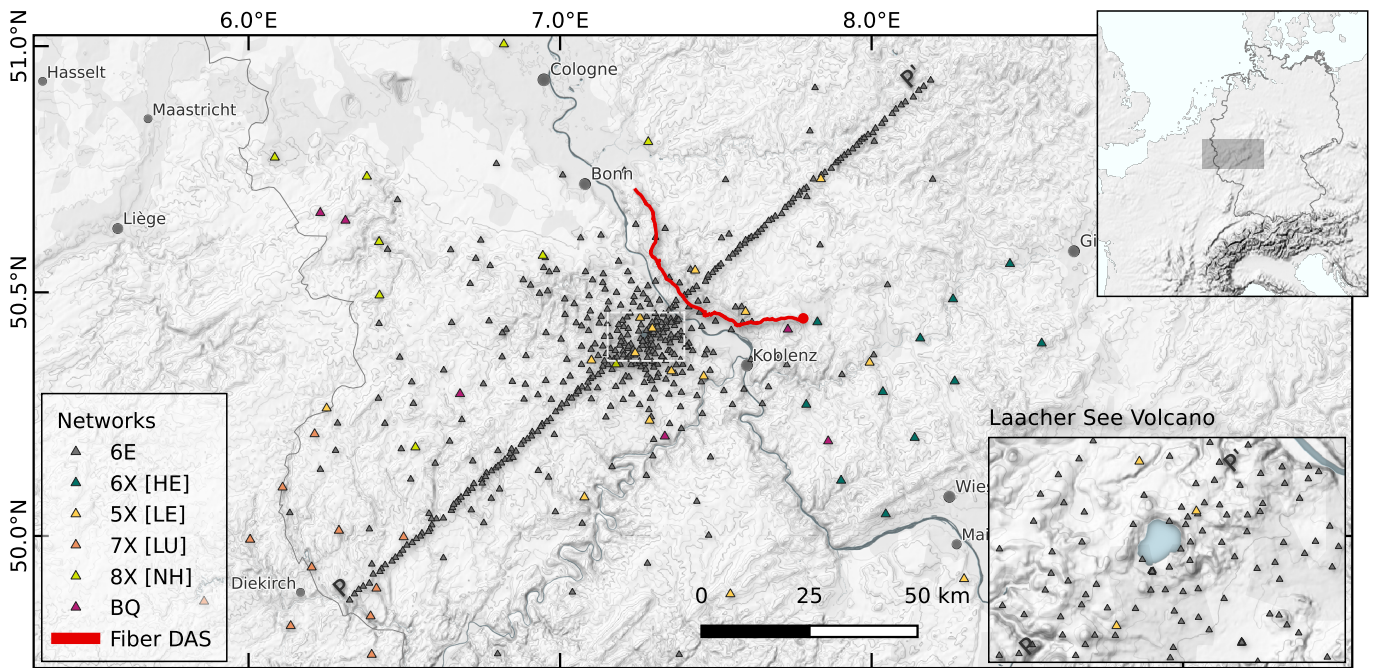
Figure 2 Layout of the temporary seismic network (6E), contributing permanent networks and the fibre optic cable for distributed acoustic sensing (DAS) deployed as part of the Eifel large-N experiment, one of the largest experiments in the Eifel so far (Dahm et al., 2023) . The temporary stations recorded from September 2022 to August 2023, and the DAS for 6 months between March and August 2023. The centre of the deployment is the Laacher See (see inset figure). The contributing networks have temporary network codes [5-8]X in brackets are the permanent names of those networks.

2 Experimental design and implementation

2.1 Network design and pre-site surveying

The experiment and network were designed with the following main objectives:

- Image crustal structure including the hypothesized remnants of the LSV magmatic reservoir below 4 km depth
- Image the characteristics of the crust-mantle transition in and around the source region of the DLF events
- Monitor tectonic and volcanic seismicity in the volcanic fields with a focus on LSV and the occurrence of DLF earthquakes

With the three kinds of instruments available to us (4.5 Hz geophones, 1 Hz seismometers and broadband seismometers) a hierarchical network with concentric areal distributions was chosen. Broadband stations with capabilities for deep imaging using low frequency surface wave tomography were distributed almost homogeneously within a circle of about 80 km radius and this network was densified by the 1 Hz sensors. This backbone network which already has some densification towards the center at the LSV was complemented by the 4.5 Hz geophones, arranged in a network with an aperture of about 60 km. In combination the network features station distances decreasing from about 10-20 km at the periphery to less then 1 km in the central location.

To accommodate the mutually exclusive requirements for high resolution crustal imaging of the LSV and

the deep imaging of the Moho, the 4.5 Hz geophones were redeployed after 6 months of recording onto a 160 km long SW-NE trending line with 1 km station distance. The orientation of the profile resulted from considerations of earlier active seismic profiles, the main structural features like Rhine valley and Siegener main thrust and the expected noise conditions with heavy human activity along the Rhine river. With redeployement of the high frequency geophones a high resolution, high-frequency imaging and seismicity monitoring of the of the LSV can be achieved with 6 month of data as well as a densely covered 2D deep crustal imaging. In both configurations the 11 months long records of the backbone network can (A) be used for continued seismicity monitoring, (B) improved Green's function recovery from noise at low frequencies, and (C) 3D extrapolation of deep imaging using the linear geophone configuration.

Extensive site surveys scouted locations and arranged contacts with property owners to prepare for effective field campaigns. Stations were installed in forests, on private properties or in buildings such as castles, mines and auxiliary buildings. The station configuration is shown in Figure 3a and consists of a DataCube digitizer, the sensor and a 9V (160 Ah) super alkaline air battery housed in a vented storage box to protect battery and digitizer from rain. While the sensors at outdoor locations were installed at a depth of about 50 cm, the box remained above the surface to provide oxygen for the battery and view to the sky for the GPS receiver that provided the timing.

On average stations were serviced after 3 months to retrieve data and renew the batteries. During the course
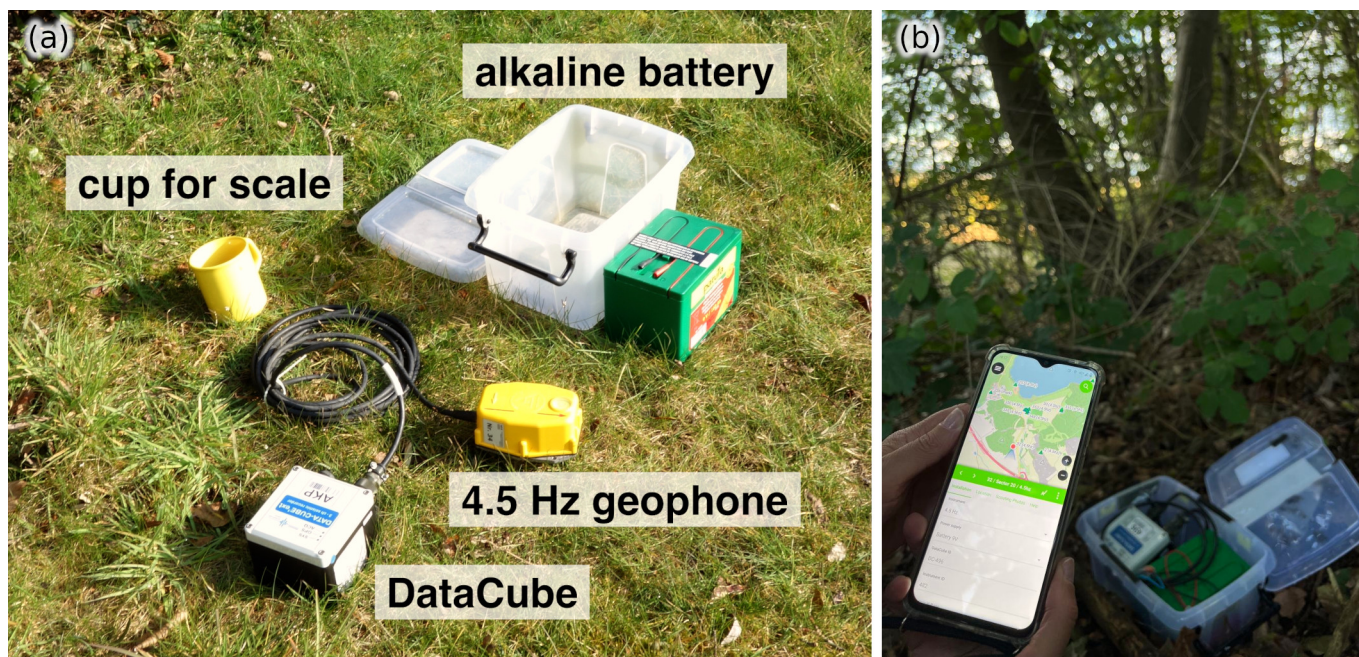
Figure 3 Configuration of a typical station (a) with a DataCube digitizer, seismic instrument (here, 4.5 Hz geophone) and a 9 V, 160 Ah super alkaline air battery. Photo (b) shows the QField GIS interface during deployment of a seismic stations.

of the experiment only around 2 % of the stations were damaged or lost.

2.2 Online GIS: Experiment Organization and Mobilization

The site information was collaboratively organized in a geographical information system (GIS), namely QGIS (QGIS Development Team, 2024). Beginning with the desired network layout on the drafting board and during the subsequent scouting phase, site information was gathered using the open-source QField mobile app (Fig. 3b). Contact information and site photos were entered into the database in the field on mobile devices. This workflow ensured a single database as a single source of truth where all information and log books of the 500+ sites was collected. The mobilisation and demobilsation fieldwork was orchestrated using the mobile QField app. Each of the 10+ field teams was equipped with a smartphone or tablet with the QField app installed, which was synchronized to the online GIS database at night. During the day, teams worked independently on assigned sectors without the need to connect to the central database, but with the possibility to commit changes if possible. The QField app provided the teams with location navigation, all relevant information, and photos of the deployment site. The field teams updated station deployment and installation information independently. At the end of each day, all updates were synchronized to the online databases using QFieldCloud infrastructure.

The online GIS workflow ensured a consistent information flow and productive, self-responsible collaboration of the fieldwork teams. Furthermore, the online database offered a real-time progress status of the deployment sectors, helping the teams be efficiently organized. The GIS database also allowed the swift organiza-

tion of the station metadata. A QField template project is provided in the supplement information.

3 Waveforms and associated databases

3.1 Data quality

Station uptimes

The median station uptime (Fig. 4) was approximately 88% of the deployment time. Downtimes were largely influenced by battery power, which depended on a number of factors: (1) health of the deployed air batteries, (2) battery degradation through humidity and performance, affected by temperature, (3) power consumption of the seismic instrument, affected by GPS availability and sampling rate. The deployed seismic instruments had different power requirements. While the broadband Trillium Compact sensors are active force-feedback instrument and were equipped with two batteries each, the passive 1 Hz (Mark) and 4.5 Hz Geophones we equipped with one battery each.

Quality control of the large-N network waveform data and metadata

The 6E network includes broadband seismometers with corner frequencies of 120 s and 20 s, 1 Hz short period stations, and 4.5 Hz geophones (Fig. 5). Station metadata of the temporary Eifel large-N network (6E) is provided in FDSN-StationXML format. The file was carefully reviewed for consistency and completeness using the stationxml-validator tool v. 1.7.5 provided by IRIS [1], last accessed July 2024). The tool proved helpful to detect (and correct) for example issues concerning start-
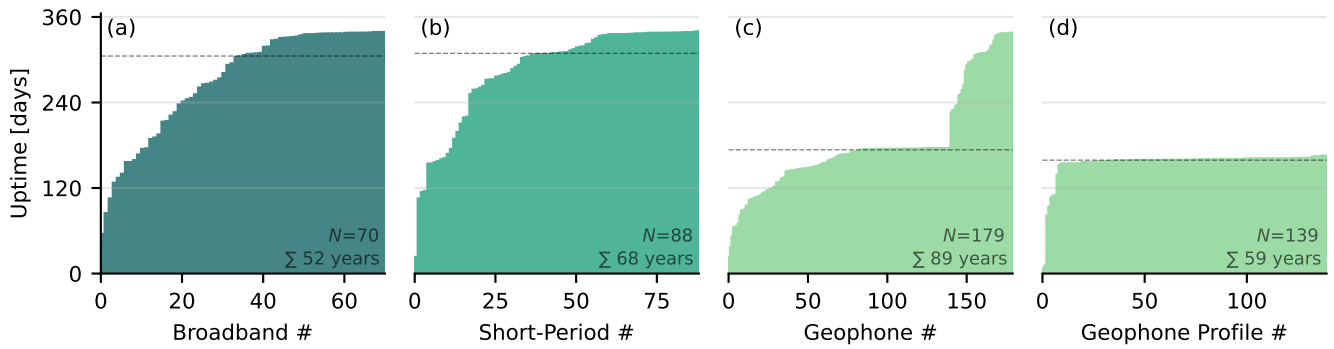
---

[1]https://github.com/iris-edu/StationXML-Validator

Figure 4 Sorted station uptimes grouped by instrument and network layout. The broadband Trillium Compact 20 s / 120 s (a) and Mark short period instruments (1 Hz) (b) were operated in the spatially extended network. The 4.5 Hz geophones were operated in the spatially extended network (c) for the first half of the experiment and then re-deployed onto the SE - NW profile (d; see Fig. 2). The dashed line indicates the median uptime of the instruments.
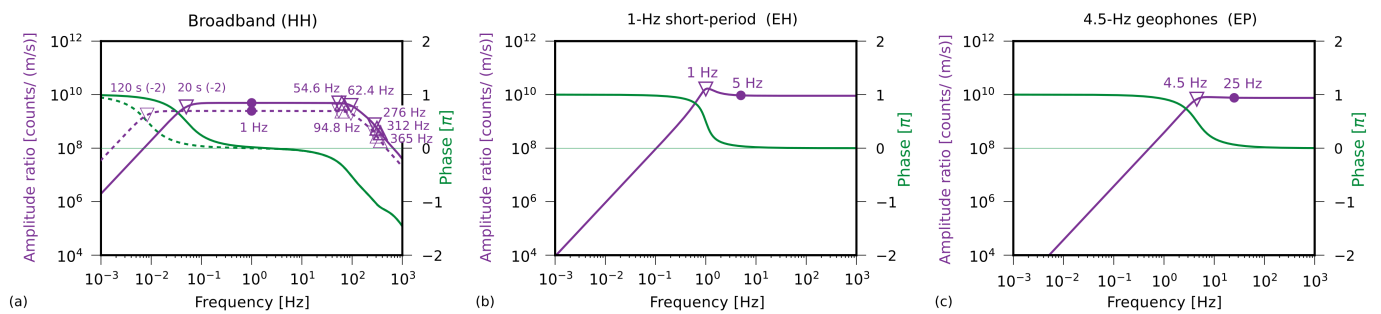

Figure 5 Responses of the three sensor types of the 6E temporary network: (a) 120 s (dashed lines) and 20 s (solid lines) broadband seismometers, (b) 1 Hz short-period sensors, and (c) 4.5 Hz geophones. Triangles mark the breakpoints of the poles and zeros response, the filled circles mark the frequency for which the sensitivity value is reported in the station-xml files. Input unit of all three instrument responses is m/s, output unit is counts.

and end-times, unit naming conventions, or missing information.

In addition to this metadata check, we applied the quality control toolbox AutoStatsQ (Petersen et al., 2019) to check (1) the horizontal sensor orientations, (2) amplitude gains, and (3) large GPS time errors ($\geq 2s$). All tests are based on waveform records of azimuthally distributed teleseismic events. Utilized frequency bands below 0.2 Hz limit the test to broadband seismometers and 1 Hz short period stations, thus excluding the 4.5 Hz geophones from the analysis. The orientation test is based on the comparison of Rayleigh wave polarization on vertical and radial components, while the amplitude gain test compares first arriving P phase amplitudes on the vertical components among the stations of the network as well as to expected amplitudes forward modeled using a global 1D velocity model. The timing test is based on cross-correlating synthetic and observed waveforms to obtain time shifts. A correction for each event is applied based on the median time shift across all stations. For detailed description of the tests see the supplementary material and Petersen et al. (2019).

The resolution of the three tests depends on the availability of high-quality waveform records of a sufficient number of teleseismic events, and therefore mainly on each station's uptime. In the supplement to this paper, we provide tables of correction values for the orientation of the horizontal components. After checking

154 broadband and short period sensors, we find and report results of 4 HH and 14 EH sensors with misorientations $\geq 20°$ for which we suggest correcting before performing sensitive seismological analysis such as moment tensor inversion or shear wave splitting analysis. The obtained orientations are provided as azimuth in the stationXML metadata and north and east channels were renamed to HH1/EH1 and HH2/EH2. For three broadband (HH) seismometers and one 1 Hz short period station we observe misorientations of 180°, corresponding to the North component pointing southward or a sign error of the horizontal channels. These four stations were corrected before publishing the dataset. The heterogeneous recording lengths of the stations is reflected in the stability of results. For about 10 % of the broadband stations and 20 % of the short period stations the number of teleseismic events with a good signal-to-noise ratio is too small to obtain meaningful results.

We conclude from our further tests, that the amplitude gain factors of all tested HH and EH stations are correct. In addition, we do not observe GPS timing errors that exceed the resolution limit of the test (2 s), but note that due to the limited operation length the test could not provide meaningful results for about 13 % of the HH and EH stations.

AutoStatsQ has previously been applied to several different networks, including for example the AlpArray, Swath-D (Petersen et al., 2019) and KOERI (Büyükakpı-

nar et al., 2021) networks. Compared to these networks, the Eifel large-N network of HH and EH stations performs similar with about 10 % misoriented stations.

Visualization of global seismic phases and event example

Dense seismic networks like the Eifel large-N experiment allow detailed observations of wave propagation. While those wavefield observations are mainly used to determine deep structures in teleseismic applications, time-dependent visualizations of the ground motions across the network can also serve as an additional health-monitoring step and for educational purpose. We use a visualization tool developed by Ling et al. (2021), adjusting the code to the Eifel large-N network, which is characterized by a significantly smaller aperture and different sensor types compared to the original use case, which was the AlpArray Seismic Network. In the supplement of this paper, we include movies of one teleseismic event (M 7.6, 2023-01-09, Banda Sea) and of the M 7.7 Türkiye earthquake (2023-02-06) at intermediate distance. The animations contain a ground motion map, one reference seismogram, a frequency-wavenumber diagram, and a ray-path plot. The analysis and plotting are based on the ObsPy seismology software (Krischer et al., 2015) and TauP travel times using the IASP91 global seismic velocity model (Kennett and Engdahl, 1991; Snoke, 2009). Details on the method and data processing are provided in the supplement file.

Local event examples

Fig. 6 shows a record section at large-N stations for a sequence of local earthquakes beneath Kruft about $10\,km$ from LSV at about $10\,km$ depth. The largest event with a magnitude ML 2.1 was preceded and followed by smaller micro-earthquakes with ML 0.4 and smaller. While individual stations show site-specific noise and the smaller pre- and aftershocks would be difficult to resolve, the shear number of records and the small distance between them helps to correlate and measure the move-out of the direct P and S arrival. The visual representation of the waveforms in Fig. 6 suggests that waveform or waveform attribute stacking methods are particularly suitable for detecting and locating very small earthquakes. This has been confirmed in initial applications, as shown below.

Fig. 7 shows the recordings of a local M_L 2.9 earthquake in $12\,km$ depth on the $64\,km$ long dark fibre interrogated by an OptoDAS acquisition system. The 5200+ channel locations of the cable ($12\,m$ channel spacing) have been geolocated by hammer blow experiments, and the metadata for the cable were constructed according to seismological conventions and additional entries in the mseed format. The strain-rate of a subset of channels is plotted after de-noising with an adaptive frequency-wavenumber filter (AFK, see, Isken et al., 2022). The arrival times of the P- and S- waves are well defined and can be modelled in a half space with $v_P \approx 6.25\,km/s$ and $v_s \approx 3.85\,km$, leading to $v_P/v_S = 1.62$. Amplitude variations along cable distance are visible, which are likely caused by a combination of geometrical

attenuation, radiation pattern and site-specific damping. Of interest are the variations in the appearance of the coda wave. These may reflect the presence or absence of irregular near surface scatterers as for instance caused by topography and valleys. At cable distances of $50\,km$ or larger (distance to the earthquake about $28\,km$) a secondary phase is clearly visible, which can be modelled as a SmS reflection from a layer in a depth of $m = 22\,km$ beneath the Laacher See volcanic system.

In Fig. 8 we show seismogram sections of the same M_L 2.9 earthquake along the SE-NW running profile in Fig. 2 with small station spacings between 1 and 2 km, both along the northeast and southwest branches. The arrival times of the direct P and S waves already show significant differences in the two segments. While the direct P-wave can be well adapted in both branches with a layer-over-half-space model with velocity $v_P = 6.7\,km/s$, the fitting of the arrival time of the direct S-wave requires a ratio $v_P/v_S = 1.7$ in the westerly direction, similar to the north direction displayed in Fig. 7, but only 1.62 in the easterly direction. Modelling of the Moho-refracted Pn propagation suggests a Moho depth of 24 km and 29.7 km in the easterly and westerly directions, respectively. Variations in Moho depth have previously been identified by refraction seismic experiments (e.g., Mooney and Prodehl, 1978; Mechie et al., 1978), including the detection of low velocity layers above and below the Moho. However, only P-waves were excited by surface explosions in these experiments, and strong surface waves challenged the interpretation of later body wave arrivals. In contrast, the data collected in the large-N allow the interpretation of S-wave reflections and show few surface waves because the earthquake sources are at depth.

The seismogram sections in Fig. 7 and 8 already show the importance of larger network apertures of 130 km and more to resolve the depth and characteristics of layer interfaces and sill-type reservoirs in the lower crust and at the Moho.

3.2 Database of empirical Green functions

Collected data were used to verify that the calculation of Empirical Green's functions (EGF) from cross correlations is possible with the mixture of stations, with positive results. The workflow to calculate cross correlations follows the approach by Bensen et al. (2007). Station pairs including 4.5 Hz sensors allow EGFs consistently down to about 8 s, often over 10 s with good signal-to-noise ratio (SNR) (Fig. 9). Pairs with 1 Hz Mark geofons can resolve signals down to roughly 30 s and pairs with Trillium compact can retrieve EGFs down to over 100 s with good SNR. Pairing 4.5 Hz sensors with Trillium compact sensors can enhance the signal in the low periods compared to only using 4.5 Hz sensors.

4 Results

4.1 Catalog of local earthquakes and station residuals

The SNR of the large-N stations is generally good (see examples in Figs. 6 and 7), so that high frequency P
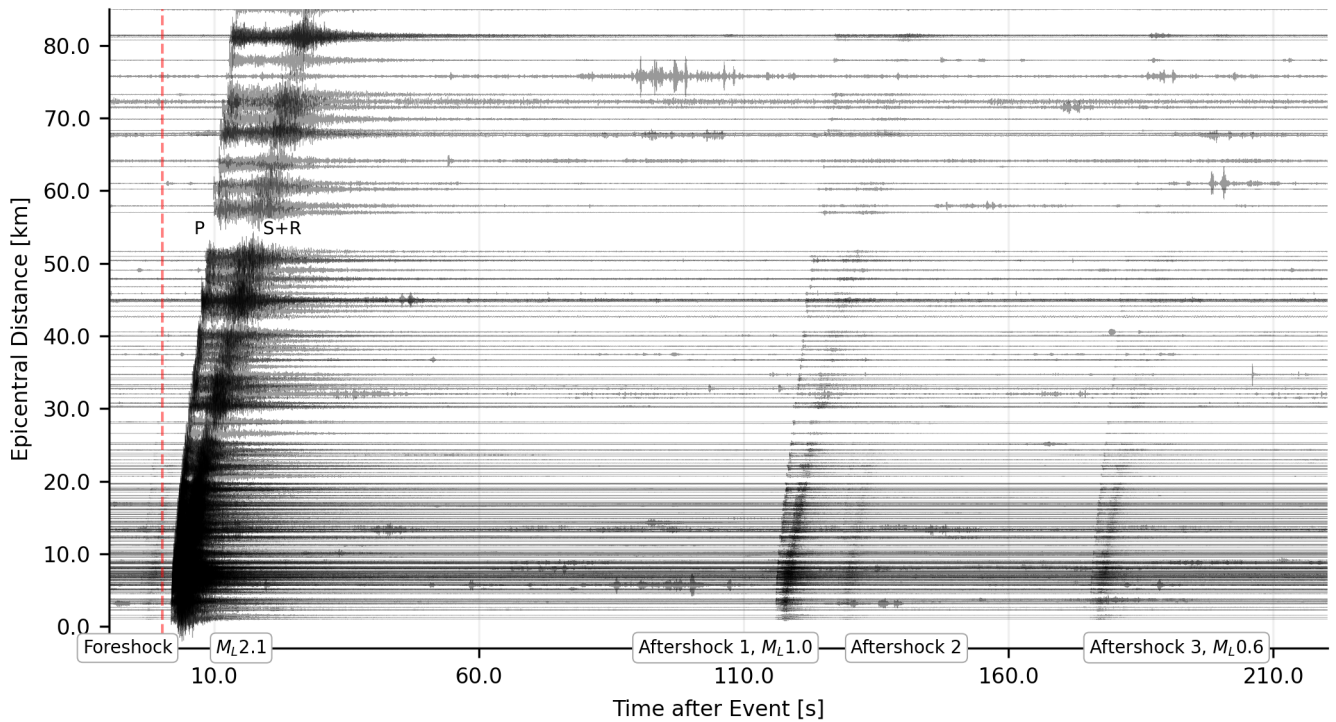
Figure 6 Record section on a part of the large-N stations (Z component) for a sequence of earthquakes beneath Kruft about 10 km from LSV at about 10 km depth. Magnitudes range from ML 2.1 to below ML 0.4. Traces are unfiltered and scaled to their maxima.
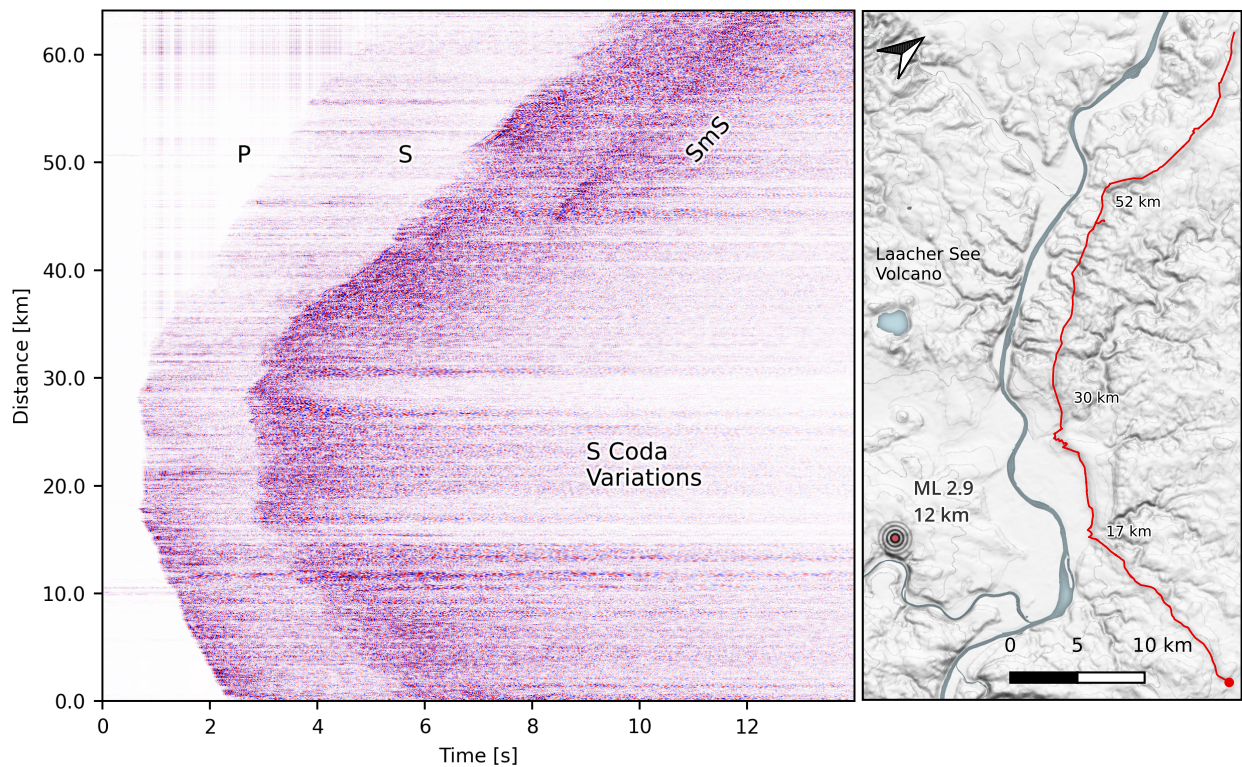

Figure 7 Example of DAS recordings of a local ML 2.9 earthquake SE of Mendig on 18 April 2023 at 1:23 AM (UTC) at about 16 km depth. The strain rate data was recorded along a 64 km fiber by an ASN OptoDAS interrogator on 5200+ channels at 12 m channel spacing with a gauge length of 16 m and a sampling frequency of 250 Hz. Distance along the cable is plotted. The seismic data has been de-noised with the AFK filter (Isken et al., 2022) and subsequently bandpass-filtered between 1 and 20 Hz. The traces are normalised to their maximum. The arrival of P, S and a late SmS reflection at m=22 km depth are indicated. The geometry of the DAS cable (red line), the interrogator (red dot) and location of the earthquake (circle) are indicated in the map on the right panel.
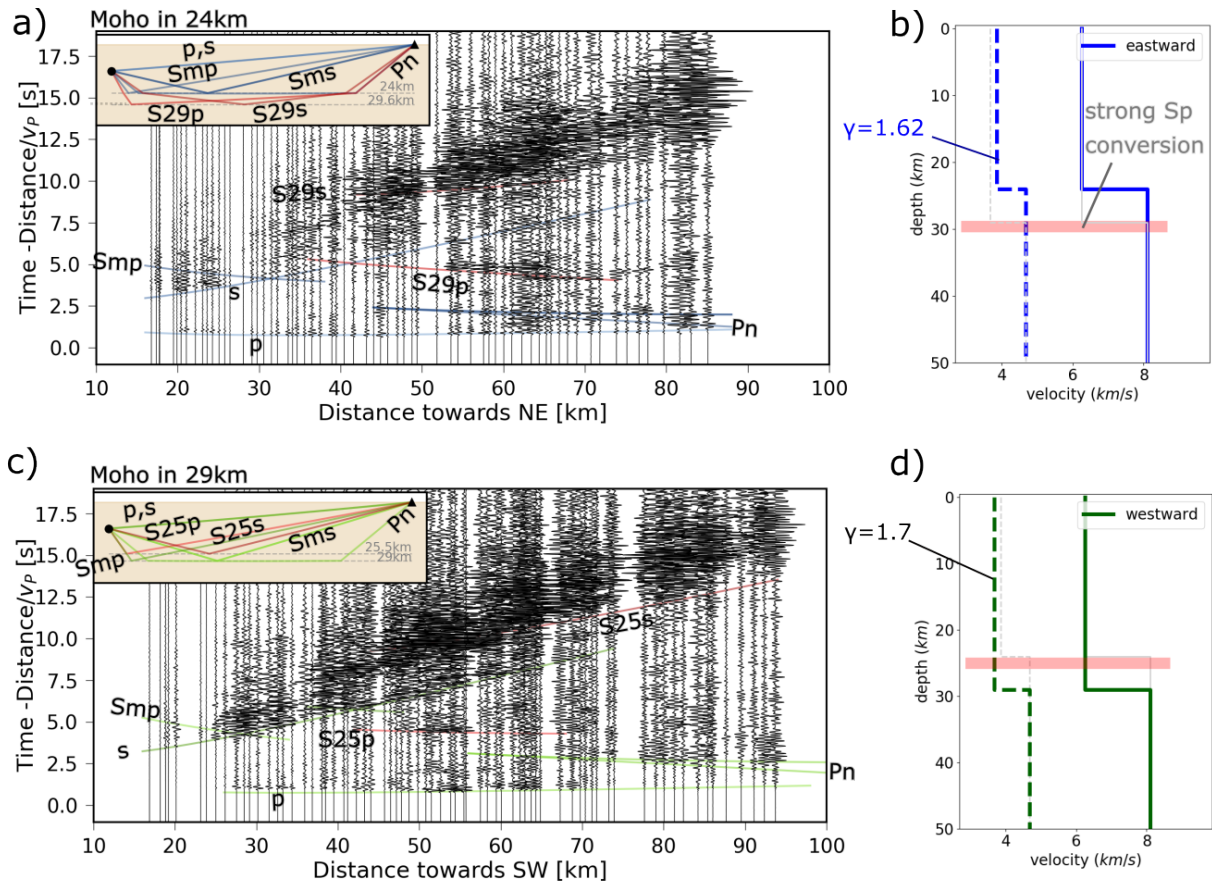
Figure 8 Seismogram sections of the magnitude 2.9 earthquake plotted in Fig. 7 along the SE-NW running profile of the geophones plotted in Fig. 2. Panel (a) shows the record section of the northeast branch of the profile and (c) of the southwest branch. The time reduction velocity was 6.7 km/s, so that the onset of the direct P-waves in the crust is horizontal. The onset of the direct S-wave can be modelled using different velocity ratios of $\gamma = v_P/v_S = 1.62$ and 1.7 in the eastern and western branches, respectively (b and d). The arrival times of the PmP and Pn phases suggest different depths of the Moho at either 24 or 29.7 km (b and d). Strong reflections arriving between the direct P- and S- waves and after the S-wave have been modelled (Pyrocko tool cake) by assuming S-to-P conversions and S-to-S reflections at 25.5 and 29.9 km depths.

and S-waves from local earthquakes down to magnitude $M = 0$ can be automatically picked.

We tested conventional versus neural network picker (e.g. STA/LTA versus Phasenet, see, Zhu and Beroza, 2018). Additionally, we compared different machine-learning (ML) based pickers. In summary, we found that ML-based pickers outperformed conventional pickers for the Eifel large-N database, and Phasenet performed best among the different ML pickers (see supplement Fig. S5). For event detection and localisation, we tested another approach as a conventional travel-time location method. Stacking waveform attributes is a very robust and reliable location method when large and dense networks can be used, with the advantage that phase association is not required. In our case, we stacked the probability functions derived from the Phasenet picker on a flexible grid of trial locations. The location with the highest semblance in the stack has the highest probability and is selected as the event location. The method is described in Isken et al. (2025). It employs a hierarchical octree data structure (Meagher, 1982) to iteratively adapt the search grid to high resolution in regions of high semblance. Further, station and source-specific correction terms, estimated from the ensemble of event locations, are considered. Event

magnitudes are obtained by comparing measured peak amplitudes with those extracted from a Green function database of synthetic seismograms (see, Dahm et al., 2024). In addition to the Eifel large-N dataset, the method has so far been successfully applied to the Reykjanes Peninsula, Iceland, (e.g., Büyükakpınar et al., 2025), the Utah FORGE (Frontier Observatory for Research in Geothermal Energy) injection experiments in SW Utah, USA (Niemz et al., 2024), and the Vogtland earthquake swarm region on the German-Czech border (Büyükakpınar et al., 2024).

The automatic location with *Qseek* retrieves quarry blasts and surface sources at the surface well if they occur in the centre of the network (Fig. 11).

Fig. 10 shows the epicenters and depths of earthquakes in the seismicity catalog generated by the *Qseek* automatic routine. Event magnitudes range from M 0 to M 2.9. Overall, more than 1200 earthquakes with $M > 0$ were detected and located with *Qseek*, while the routine location of the Seismological Survey located only about 198 earthquakes during the same period. The seismic catalog has already brought some surprises and new insights. Most of the earthquakes occurred in a depth range between 10 and 14 km in the Ochtendung seismic zone in the Neuwied basin, confirming the pattern
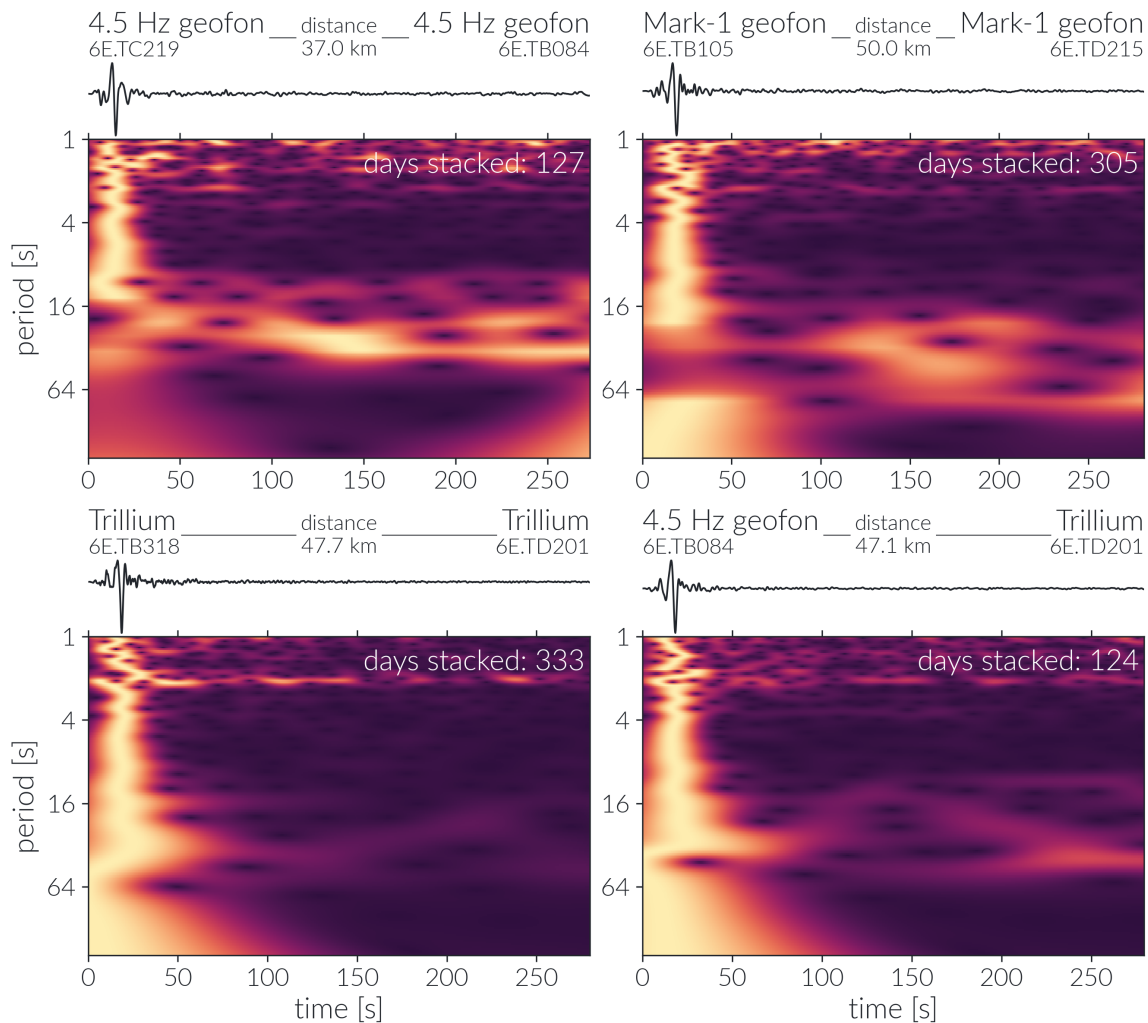
Figure 9 Examples for cross correlation functions for several station pairs in the Eifel large-N dataset. Different sensor combinations allow for different signal resolutions in the lower frequencies. The examples shown compare different pairs (4.5 Hz geophones, 1 Hz Mark geophones, Trillium compact broadband seismometers and the combinations with one 4.5 Hz geophone and one Trillium compact broadband seismometer) with roughly the same orientation of the inter-station path within the network. The cross correlation trace is shown with the spectrogram.

of previous years. However, unlike in previous years, clusters of earthquakes occurred directly beneath the three volcanic centers, Laacher See, Rieden and Wehr, at depths between 11 and 8 km. Also new is the detection of crustal micro-earthquakes in the WEVF, which has not been documented before.

An important question for large-N experiments is whether the ML-based P and S picks and the automatic *Qseek* locations can be used for joint tomography. Figure 12 shows the residual P-wave arrival times for all events in our catalogue. Strong delays up to -0.5 s occur in the EEVF near Laacher See. Similar patterns are observed for S-waves. This suggests that 3D tomography will have the resolution to resolve the velocity structure in the uppermost 15 km beneath the LSV.

4.2 Feasibility of nodal array receiver function analysis

Passive-source seismic imaging using the receiver function (RF) method is commonly used to investigate the structure in the crust and upper mantle. Conventional

RFs are calculated from broadband data and are usually stacked over a large number of teleseismic events to enhance the SNR. Short-period stations have proven successful in extracting proper RFs (e.g., Yuan et al., 1997), and their use has increased significantly in recent years (e.g., Ward and Lin, 2017). Here we show that it is feasible to apply RF analysis to our large-N experiment in the Eifel and that it is also possible to obtain RFs of reasonable quality from an event.

A teleseismic earthquake of magnitude 6.5 occurred on 2022-09-17 southeast of Taiwan and was well recorded by most of our stations. The event was located ~87° away from the seismic network with a back azimuth of ~57°. While the P-waves are easily detectable in the original recordings from the broadband Trillium Compact stations (Fig. 13, left panel, traces 1-3), the waveforms are less visible at the short-period Mark L4 stations (traces 4-6) and are undetectable at the geophone stations (traces 7-9). After removing the instrument response and high-pass filter, the P-waveforms become clearly visible in the displacement data from all types of instruments (Fig. 13, right panel).
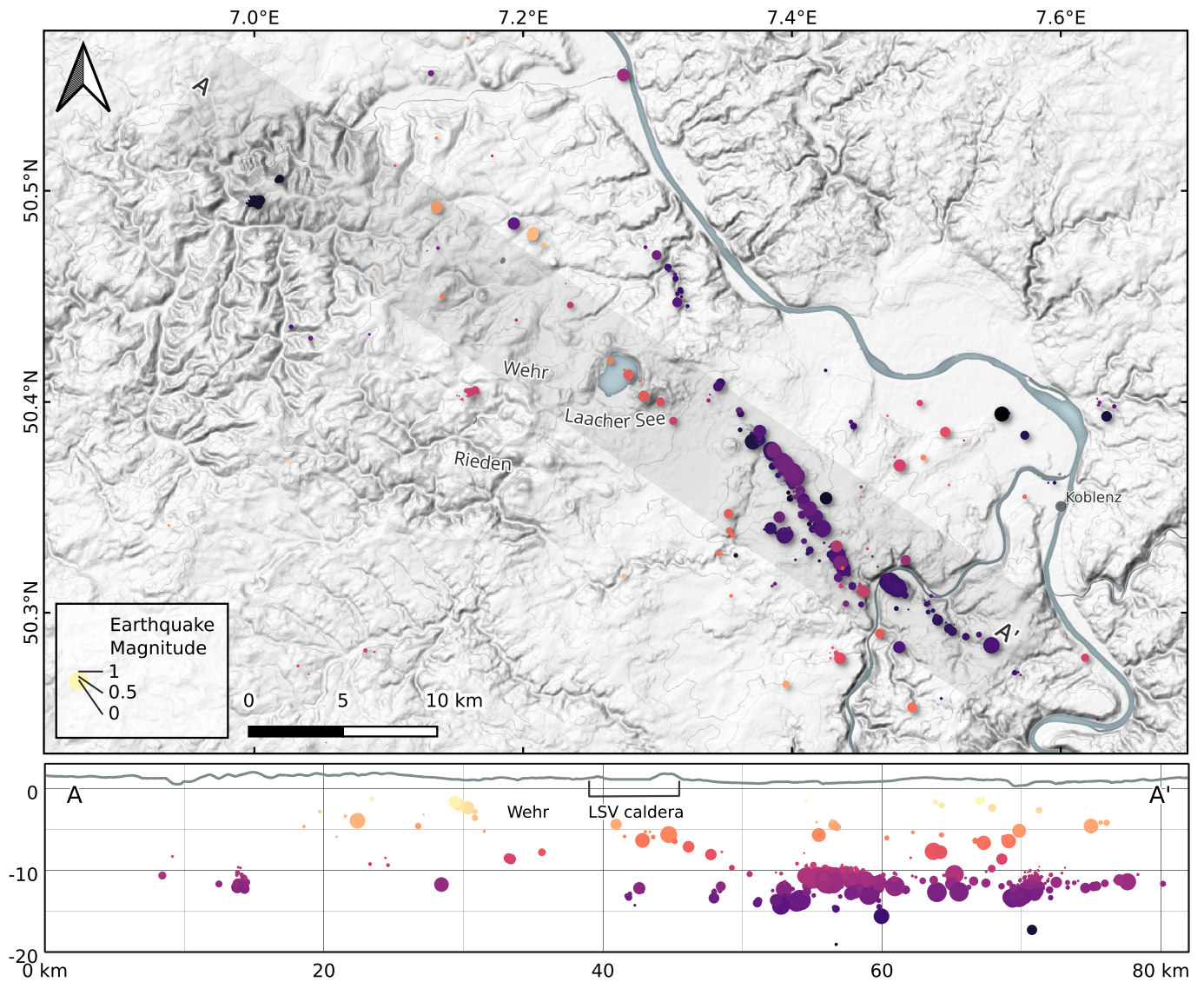
Figure 10 Earthquakes between September 2022 and September 2023 automatically located with *Qseek*. Magnitudes are indicated by size of circles (see legend), and earthquake depths are indicated by colours (see cross section). The dashed profile A-A' crosses the LSV caldera. Earthquakes plotted in the depth section between A-A' (lower panel) were projected from $\pm 5\,km$ onto the profile.

Fig. 14 shows the RFs calculated from the displacements of the 2022-09-17 earthquake. It is known that individual RFs calculated from one single event are usually noisy and therefore stacking of RFs from many events is necessary to increase the SNR. However, in Fig. 14, most of the RFs are of high quality and exhibit consistent converted phases from the crust and upper mantle discontinuities. RFs from short-period stations, especially of the geophones are comparable to those from the broadband stations. Geophone receiver functions also often benefit from the greater station density, which can result in a higher SNR in their stack than broadband stations.

Fig. 15 is the common conversion point (CCP) stacked RF image along a profile from southwest to northeast. Four events that occurred from September 2022 to March 2023 with magnitudes larger than 6.0 are used. This is the time frame of the first phase of the experiment, where only areal array stations were deployed (see station map in Fig. 15). Several interfaces can be de-

picted in the RF image. An interface at shallow depths down to $\sim 5\,km$ may represent the crystalline basement. The Moho is clearly imaged at depths between 20 and 30 km. Below the Laacher See, where the DLF earthquakes are located, the Moho is updoming to a depth of $\sim 25\,km$. The Moho depth variation generally agrees with previous RF studies showing a shallow Moho in the area (Budweg et al., 2006; Seiberlich et al., 2013). The image also reveals a discontinuity at depths around $60\,km$ with a negative velocity gradient. This interface may represent the lithosphere-asthenosphere boundary (LAB) and is consistent with a LAB depth of $60\,km$ reported by a previous RF study (Seiberlich et al., 2013) and with a surface wave study showing a low velocity zone at depths below $\sim 70\,km$ (Mathar et al., 2006). In our RF image the LAB interface is elevated to $\sim 55\,km$ below Laacher See.
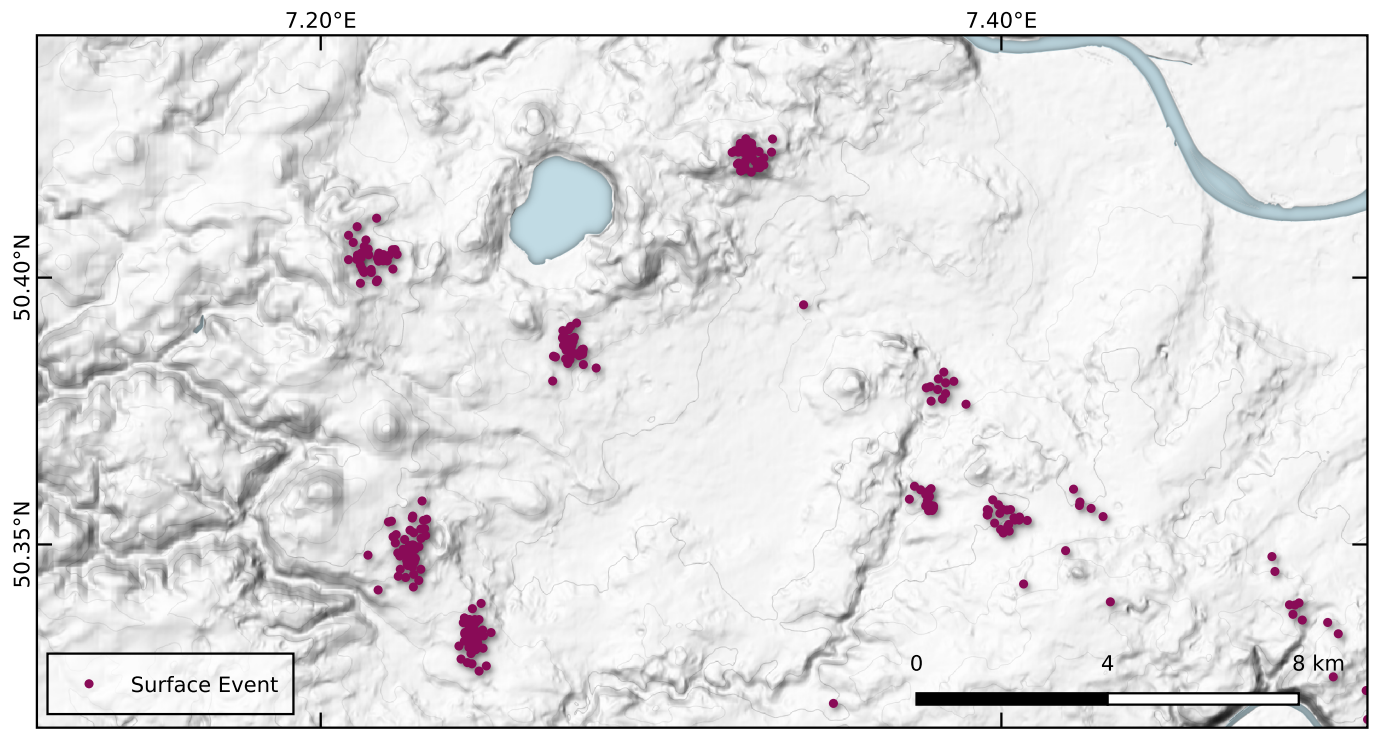
Figure 11 Plotted are all earthquake locations with source depth $< 500\,m$. Clustered events coincide with known quarries, confirming the quality of the automatic neural network picking and location approach by *Qseek* (Isken et al., 2025).
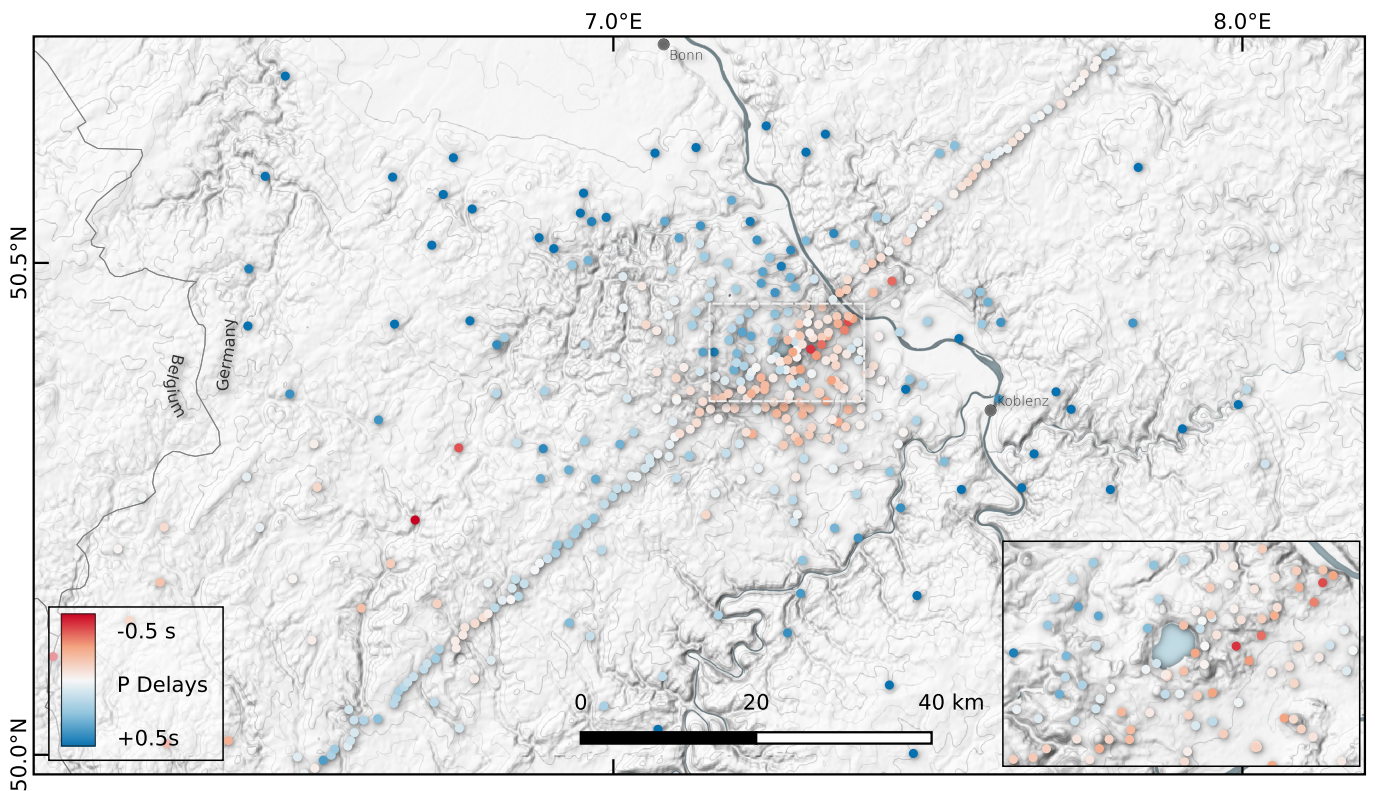

Figure 12 Mean delay times obtained from *Qseek*, which were used as station corrections in a subsequent inversion run.

4.3 Feasibility of nodal array shear wave splitting analysis

Mantle flow may cause dislocation creep of mantle minerals which, in turn, leads to crystallographic preferred orientation (CPO) of minerals, producing seismic anisotropy of the bulk mantle (e.g., Nicolas and Christensen, 1987). CPO may also be present as fossilized anisotropy from the last tectonic episode. Layers with alternating velocities or melt-filled lenses may cause shape-preferred anisotropy (SPO) in the mantle or crust. This can be measured via shear-wave splitting (SWS). When a shear-wave travels through an anisotropic medium, it is split into a fast and slow
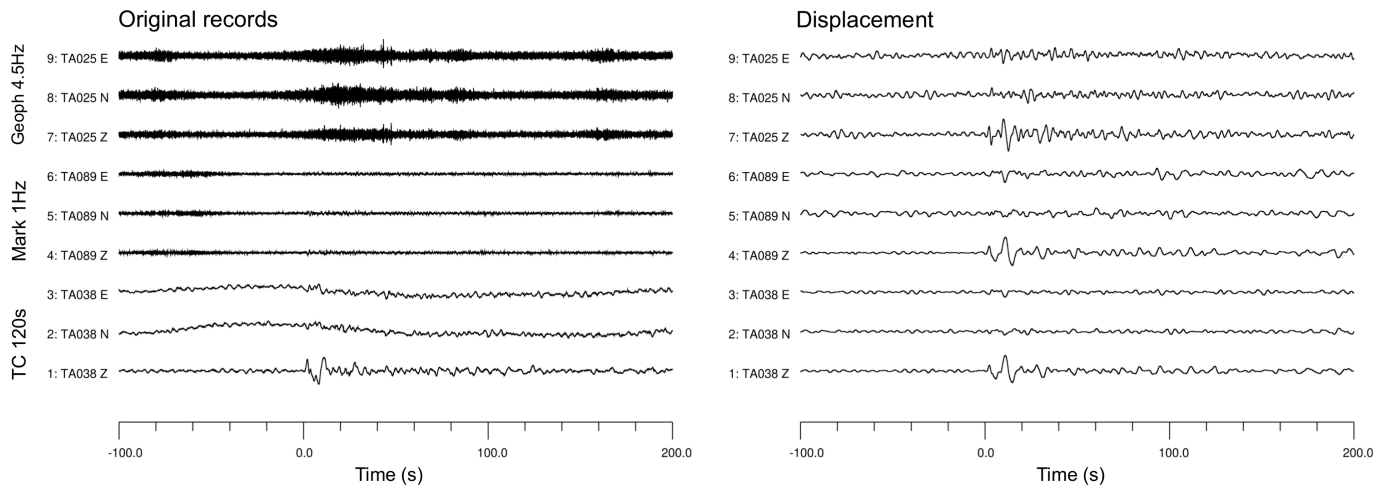
Figure 13 Example of teleseismic waveforms recorded at 3 different types of stations. Left panel shows the original records of the September 17, 2022 event (mb=6.5, dist=87°, baz=57°). The right panel shows corresponding displacement traces after removing the instrument response and high pass filter (10 s for the TC and Mark and 5 s for the geophone). The displacements for the short-period Mark and geophone stations are then clearly visible and comparable to those of the broadband stations.
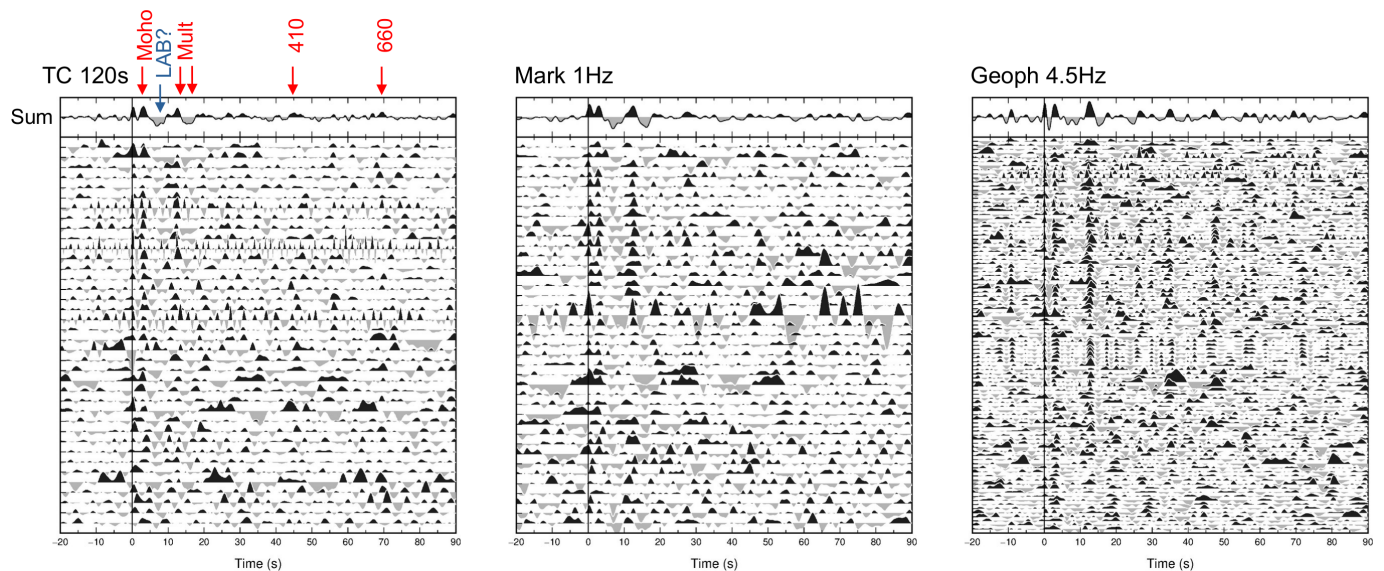

Figure 14 RFs at different types of stations calculated with the same event as shown in Fig. 13. A summation trace is shown at top of each panel. The RFs are similar for each type of instrument. The Moho converted phases and multiples are clearly visible. The upper mantle discontinuities, as well as a possible phase from the LAB are also detectable.

wave component, where the polarization of the fast wave indicates the "fast direction" ϕ of the anisotropic medium. The delay time δt between the two waves is related to the strength and/or thickness of the anisotropic medium (e.g., Silver and Chan, 1991). A prior study centered on the Eifel region interpreted SWS results due to parabolic asthenospheric flow caused by the postulated Eifel plume (Walker et al., 2005). Using the automated version of SplitRacer (Link et al., 2022), an SWS analysis tool, on our dataset, we show SWS measurements from a single M7 event on 14th September 2022, 11:04 from southeast of the Loyalty Islands [-21.1909, 170.2666]. These measurements show a uniformly ENE/WSW ϕ of 70° and mean δt of 1s. Among those, half of the measurements were made on data from 4.5 Hz geophones, with the remainder split between broadband and short-period instruments. This demonstrates that even 4.5 Hz geophone data can be

used when noise conditions are favorable. Though SWS studies usually benefit from long experiment run-times, using a single event measurement can still be insightful if the station spacing is small enough as any differences in SWS across stations can be attributed to different anisotropic structures in the subsurface. For the example shown here, fast axes are uniformly parallel to Variscan structures. Walker et al. (2005) observed many null-measurements which they assumed were likely not caused by the absent anisotropy, but the result of the fast axes being parallel to the backazimuth of the incoming wave. They concluded that, likely, there was anisotropy with a fast axis of 70° or 250° present, which is the direction of the fast polarization found in our measurement. They also reported some very large delay time δt of up to 2.4s which, considering their splitting examples (see Fig 3 of Walker et al., 2005), are rather close to null-measurements. Their preferred model of
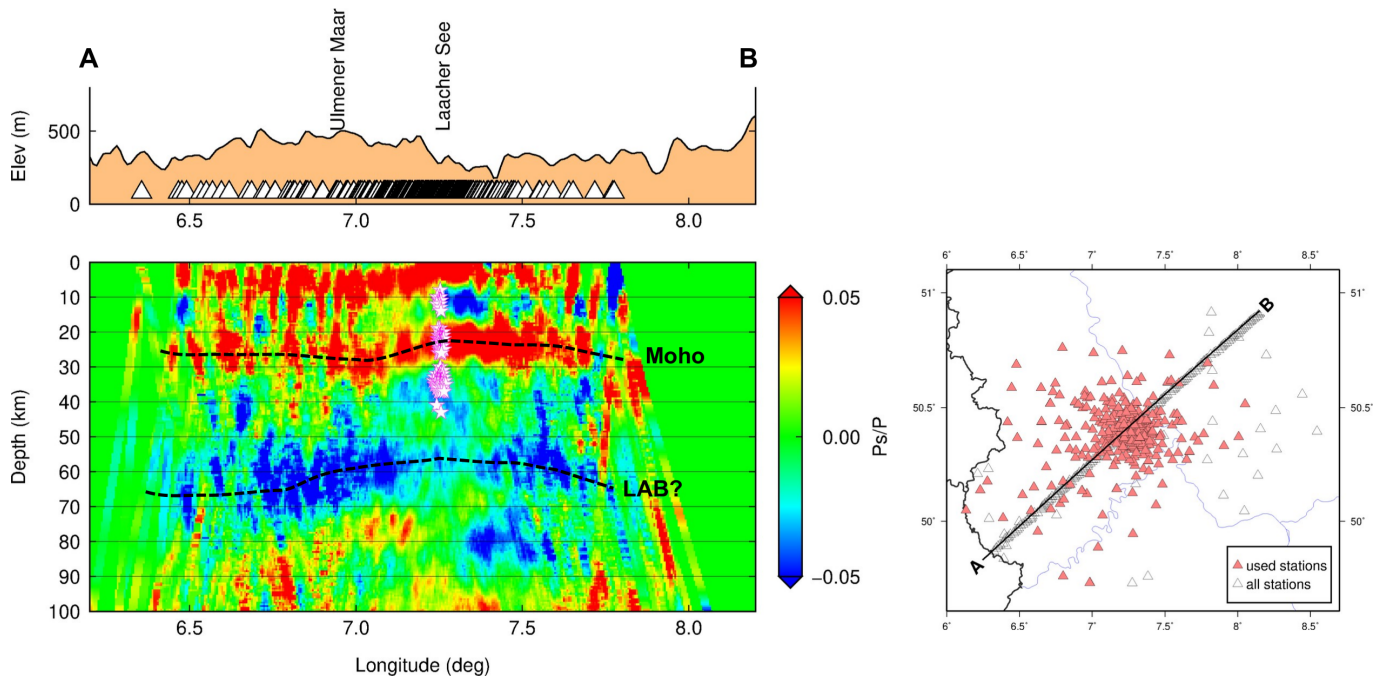
Figure 15 RF CCP image along a profile from southwest to northeast. The stations involved are from the areal array in experiment phase 1 and are highlighted in the station map. The DLF earthquakes are indicated by magenta stars. Dashed lines mark the Moho and the possible LAB phases.
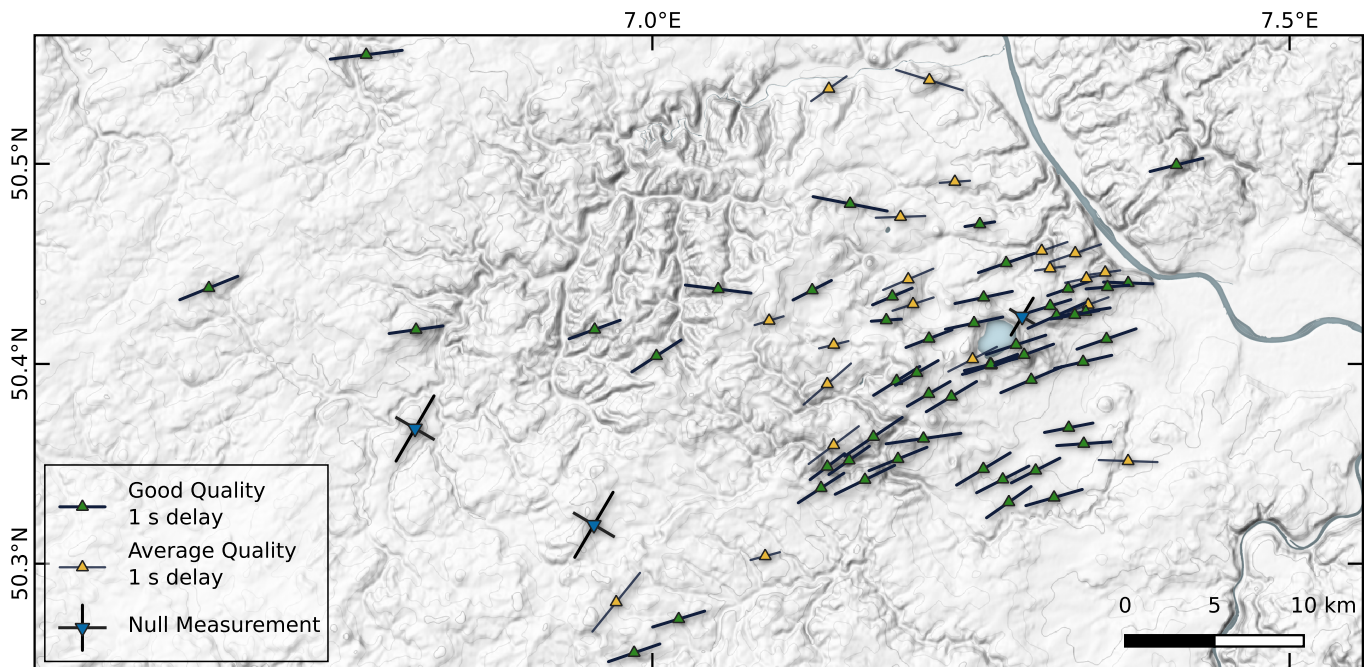

Figure 16 The results of the SWS analysis of the event on 14th September 2022, 11:04 from southeast of the Loyalty Islands [-21.1909, 170.2666]

asthenospheric flow can presently not be corroborated, as it is largely based on measurements in areas not covered by the one event we show here. In summary, the concept of using large-N high-frequency nodal arrays with a deployment time of one year is successfully contributing to anisotropy studies in the upper mantle and crust.

5 Discussion and Conclusion

The structure of a large-N network depends crucially on the scientific questions that are to be addressed. The study of distributed volcanic fields requires both high resolution from the upper mantle to the Earth's surface and extensive coverage of fields up to several thousand square kilometres in size. For the Eifel, we opted for a large-N network of buried, stand-alone three-component stations of different types (broadband, short-period, and 4.5 Hz) in combination with

small-scale arrays and close-meshed seismic and DAS-born long profiles. Station densities were very high along the long profiles and in the central area of the volcanic fields at distances of about $1\,km$ and increased systematically with distance from the centre. The broadband sensors, on the other hand, were evenly distributed over the entire study area. In retrospect, it is interesting to ask whether the design of the network meets the scientific requirements well or whether future experiments should be designed differently. We discuss this question in terms of the automatic detection and localisation of micro-earthquakes, the calculation of empirical Green's functions with sensitivity over a large depth range, the feasibility of local earthquake tomography, and the potential to perform broadband seismological analysis.

The detection and location of micro-earthquakes using the large-N deployment in combination with ML-based picker and waveform attribute migration methods was successful, as four times more earthquakes were located with small uncertainties. The arrival-time picks are of high quality and have on the one hand been used to develop detailed station correction terms and on the other hand they can be used used as direct input to local earthquake tomography (LET) studies, which could resolve the upper crustal structure beneath this region.

The empirical Greens functions between station pairs, extracted from the continuous background noise at the participating stations, are independent of local earthquakes and can be used to constrain tomographic models of the subsurface. A key question is whether the combination of different station types, e.g. broadband, short period, and 4.5 Hz geophones, is suitable for this task. We analysed noise cross-correlations at different pairs of stations at different distances. Station pairs with 4.5 Hz sensors retrieve EGFs with good SNR with periods of at least 8 s. Pairs with 1 Hz Mark geophones can resolve periods up to 30 s, and pairs with Trillium over 100 s with good SNR. Pairing 4.5 Hz sensors with Trillium compact sensors enhances the signals compared to using 4.5 Hz sensors alone.

Displacement RFs computed for single teleseismic events were of good quality, demonstrating the feasibility of RF studies even with short periods and dense arrays of 4.5 Hz sensors. CCP stacked RF images along profiles show multiple interfaces at shallow depths down to 5 km in the crust and indicate upwelling Moho and upwelling LAB boundaries beneath the EEVF, consistent with previous RFs.

Shear wave splitting analysis typically relies on broadband sensors with long deployment times. Here we tested whether the short deployment time of the large-N experiment and the use of short-period sensors is feasible. An exploratory analysis based on a single earthquake yielded a very consistent result of SKS splitting with fast axes uniformly oriented parallel to the Variscan structures. This result challenges previous interpretations of upper mantle anisotropy in the Eifel region and calls for further analysis and modelling studies.

Exploitation of the massive data from large-N experiments depends critically on the accessibility, availability, and quality of continuous waveform data. Data quality starts with the planning and documentation of station locations, acquisition parameters and stationXML files. We have had a very positive experience with an open-source GIS-based system used in the field to orchestrate the station deployments of different teams. In addition to metadata checks, we used a quality control toolbox to check horizontal sensor orientation, amplitude gains, and GPS timing errors. We also recommend generating ground motion videos for visual control of data quality. Finally, a lesson learned from our experiment is that the generation of a virtual network and a continuous waveform database is a huge effort and should be started as soon as possible after station recovery.

In conclusion, the large-N and DAS data collected in the Eifel region, together with the permanent seismic networks, provide a unique dataset with unprecedented station density and ray coverage. This allows for the first time to image the upper crustal magmatic system and the residual magma reservoirs beneath the phonolitic centres of the EEVF at high resolution. Imaging can be achieved both by dense spatial mapping or tomographic inversion of integral parameters of seismic wavefields, such as travel times or amplitude attenuation, and by analysis of the wavefronts emitted by real or virtual (e.g. reflections and transformations) seismic sources. The latter is of particular interest when local earthquakes emit S waves, to allow the study of S-reflected and Sp-converted waves at sill-type reservoirs in the lower crust. The network structure, which is being tested for the first time, is well suited for the application of established broadband seismological methods and for the performance of advanced ambient seismic noise and local earthquake tomography.

Conflict of competing interests

The authors declare that the research was conducted in the absence of any commercial or financial relationships that could be construed as a potential conflict of interest.

Acknowledgments

Data and Resources

The stations were provided by the German Instrument Pool Potsdam (GIPP) under Grant No 202216. The waveform data are archived under a Virtual Network 6E amd 6X at GEOFON database (Dahm et al., 2023). Software used to analyze data has been cited in the individual chapters. RF and SKS analysis was performed with in-house developed codes. Plotting was done using QGIS, matplotlib, matlab or gmt.

References

Alohali, A., Bertin, D., de Silva, S., Cronin, S., Duncan, R., Qaysi, S., and Moufti, M. Spatio-temporal forecasting of future volcanism at Harrat Khaybar, Saudi Arabia. *Journal of Applied Volcanology*, 11(12):0–0, 2022. doi: https://doi.org/10.1186/s13617-022-00124-z.

Bensen, G. D., Ritzwoller, M. H., Barmin, M. P., Levshin, A. L., Lin, F., Moschetti, M. P., Shapiro, N. M., and Yang, Y. Processing seismic ambient noise data to obtain reliable broad-band surface wave dispersion measurements. *Geophysical Journal International*, 169(3):1239–1260, 06 2007. doi: 10.1111/j.1365-246X.2007.03374.x.

Berndt, J. and Klemme, S. Origin of carbonatites—liquid immiscibility caught in the act. *Nature communications*, 13(1):1–8, 2022. doi: https://doi.org/10.1038/s41467-022-30500-7.

Berndt, J., Holtz, F., and Koepke, J. Experimental constraints on storage conditions in the chemically zoned phonolitic magma chamber of the Laacher See Volcano. *Contrib Mineral Petrol*, 140:469–486, 2001. doi: https://doi.org/10.1007/PL00007674.

Bourdon, B., Zindler, A., and Wörner, G. Evolution of the Laacher See magma chamber: Evidence from SIMS and TIMS measurements of U - Th disequilibria in minerals and glasses. *Earth and Planetary Science Letters*, 126:75–90, 1994. doi: https://doi.org/10.1016/0012-821X(94)90243-7.

Budweg, M., Bock, G., and Weber, M. The Eifel Plume—imaged with converted seismic waves. *Geophysical Journal International*, 166:579–589, 2006. doi: https://doi.org/10.1111/j.1365-246X.2005.02778.x.

Büyükakpınar, P., Aktar, M., Petersen, G. M., and Köseoğlu, A. Orientations of broadband stations of the KOERI seismic network (Turkey) from two independent methods: P-and Rayleigh-wave polarization. *Seismological Research Letters*, 92(3):1512–1521, 2021. doi: 10.1785/0220200362.

Büyükakpınar, P., Dahm, T., Isken, M., Hainzl, S., Ohrnberger, M., Doubravová, J., Wendt, S., Funke, S., and Fischer, T. Seismic Activity and Fluid Dynamics in the NW Bohemia/Vogtland Swarm Region. In *39th General Assembly of the European Seismological Commission (GA ESC)*, Corfu, Greece, 2024.

Büyükakpınar, P., Isken, M. P., Heimann, S., Dahm, T., Kühn, D., Starke, J., López Comino, J. ⊠ Cesca, S., Doubravová, J., Gudnason, E. ⊠ and Ágústsdóttir, T. Understanding the Seismic Signature of Transtensional Opening in the Reykjanes Peninsula Rift Zone, SW Iceland. *Journal of Geophysical Research: Solid Earth*, 130(1):e2024JB029566, 2025. doi: https://doi.org/10.1029/2024JB029566.

Caricchi, L., Sheldrake, T., and Blundly, J. Modulation of magmatic processes by CO2 flushing. *Earth Plan. Sci. Lett.*, 491:160–171, 2018. doi: https://doi.org/10.1016/j.epsl.2018.03.042.

Dahm, T., Stiller, M., Mechie, J., Heimann, S., Hensch, M., Woith, H., Schmidt, B., Gabriel, G., and Weber, M. Seismological and Geophysical Signatures of the Deep Crustal Magma Systems of the Cenozoic Volcanic Fields Beneath the Eifel, Germany. *Geochemistry, Geophysics, Geosystems*, 21(9):e2020GC009062, 2020. doi: https://doi.org/10.1029/2020GC009062.

Dahm, T., Isken, M., Milkereit, C., Mikulla, S. Yuan, X., Sens-Schönfelder, C., Meier, T., Eckel, F., Reiss, M., Rümpker, G., Zeckra, M., Carrasco, S., Hensch, M., Schmidt, B., Oth, A., and Busch, S. Eifel Large-N Seismic Network (ELSN). GFZ Data Services. Dataset/Seismic Network. 2023. doi: 10.14470/1R080930.

Dahm, T., Kuehn, D., Cesca, S., Isken, M. P., and Heimann, S. Earthquake Moment Magnitudes from Peak Ground Displacements and Synthetic Green's Functions. *Seismica*, 2024. doi: 10.26443/seismica.v3i2.1205.

Hensch, M., Dahm, T., Ritter, J., Heimann, S., Schmidt, B., Stange, S., and Lehmann, K. Deep low-frequency earthquakes reveal ongoing magmatic recharge beneath Laacher See Volcano (Eifel, Germany). *Geophysical J. Int.*, 216(3):2025–2036, 2019. doi: doi.org/10.1093/gji/ggy532.

Isken, M., Niemz, P., Münchmeyer, J., Büyükakpınar, P., Heimann, S., Cesca, S., Vasyura-Bathke, H., and Dahm, T. Qseek: A data-driven Framework for Automated Earthquake Detection, Localization and Characterization. *Seismica*, 4(1), 2025. doi: 10.26443/seismica.v4i1.1283.

Isken, M. P., Vasyura-Bathke, H., Dahm, T., and Heimann, S. Denoising distributed acoustic sensing data using an adaptive frequency–wavenumber filter. *Geophysical Journal International*, 231(2):944–949, 06 2022. doi: 10.1093/gji/ggac229.

Kennett, B. and Engdahl, E. Traveltimes for global earthquake location and phase identification. *Geophysical Journal International*, 105(2):429–465, 1991.

Kreemer, C., Blewitt, G., and Davis, P. M. Geodetic evidence for a buoyant mantle plume beneath the Eifel volcanic area, NW Europe. *Geophysical Journal International*, 222(2):1316–1332, 05 2020. doi: 10.1093/gji/ggaa227.

Krischer, L., Megies, T., Barsch, R., Beyreuther, M., Lecocq, T., Caudron, C., and Wassermann, J. ObsPy: A bridge for seismology into the scientific Python ecosystem. *Computational Science & Discovery*, 8(1):014003, 2015.

Ling, O. K. A., Stähler, S. C., Giardini, D., and AlpArray Working Group. Visualizing global seismic phases with AlpArray. *Seismological Society of America*, 92(6):3845–3855, 2021. doi: 10.1785/0220210046.

Link, F., Reiss, M., and Rümpker, G. An automatized XKS-splitting procedure for large data sets: Extension package for SplitRacer and application to the USArray. *Computers and Geosciences*, 158(104961), 2022. doi: 10.1016/j.cageo.2021.104961.

Mathar, J., Ritter, J., and Friederich, W. Surface waves image the top of the Eifel plume. *Geophysical Journal international*, 164:579–589, 2006. doi: https://doi.org/10.1111/j.1365-246X.2006.02835.x.

Meagher, D. Geometric modeling using octree encoding. *Computer Graphics and Image Processing*, 19(2):129–147, 1982. doi:

10.1016/0146-664X(82)90104-6.

Mechie, J., Prodehl, C., Fuchs, K., Kaminski, W., Flick, J., Hirn, A., Ansorge, J., and King, R. Progress report on the Rhenish Massif seismic experiment. Tectonophysics. *Tectonophysics*, 90: 215–230, 1978.

Mooney, W. and Prodehl, C. Crustal Structure of the Rhenish Massif and Adjacent Areas: a Reinterpretation of Existing Seismic-Refraction Data. *J. Geophys.*, 44:573–601, 1978.

Nicolas, A. and Christensen, N. Formation of anisotropy in upper mantle peridotites-a review. *Composition, Structure and Dynamics of the Lithosphere-Asthenosphere System*, 16:111–123, 1987.

Niemz, P., McLennan, J., Pankow, K. L., Rutledge, J., and England, K. Circulation experiments at Utah FORGE: Near-surface seismic monitoring reveals fracture growth after shut-in. *Geothermics*, 119:102947, 2024. doi: 10.1016/j.geothermics.2024.102947.

Pappalardo, L., Buono, G., Fanara, S., Yi, J., Shan, X., Guo, Z., ..., and Ventura, G. The role of CO2 flushing in triggering the 'Millennium' eruption and recent unrests at Changbaishan volcano (China/North Korea). *International Geology Review*, pages 1–14, 2022. doi: https://doi.org/10.1080/00206814.2022.2065544.

Petersen, G. M., Cesca, S., Kriegerowski, M., and the AlpArray Working Group. Automated Quality Control for Large Seismic Networks: Implementation and Application to the AlpArray Seismic Network. *Seismological Research Letters*, 90(3):1177–1190, 2019. doi: 10.1785/0220180342.

QGIS Development Team. *QGIS Geographic Information System*. QGIS Association, 2024. https://www.qgis.org.

Reinig and et al. Precise date for the Laacher See eruption synchronizes the Younger Dryas. *Nature*, 595:66–69, 2021. doi: https://doi.org/10.1038/s41586-021-03608-x.

Rout, S. and Wörner, G. Zoning and exsolution in alkali feldspars from the LSV: constraints on temperature history prior to eruption. *Contr. Mineral. Petrol.*, 2018. doi: 10.1007/s00410-018-1522-x.

Rout, S. S. and Wörner, G. Constraints on the pre-eruptive magmatic history of the Quaternary Laacher See volcano (Germany). *Contr. Mineral. and Petrol.*, 175(73), 2020. doi: 10.1007/s00410-020-01710-3.

Schmitt, A., Wetzel, F., Cooper, K., Zou, H., and Wörner, G. Magmatic longevity of Laacher See Volcano (Eifel, Germany) indicated by intrusive carbonatites. *J Petrol.*, 50:1053–1085, 2010. doi: https://doi.org/10.1093/petrology/egq011.

Seiberlich, C., Ritter, J., and Wawerzinek, B. Topography of the lithosphere–asthenosphere boundary below the Upper Rhine Graben Rift and the volcanic Eifel region, Central Europe. *Tectonophysics*, 603:222–236, 2013. doi: http://dx.doi.org/10.1016/j.tecto.2013.05.034.

Silver, P. and Chan, W. Shear wave splitting and subcontinental mantle deformation. *Journal of Geophysical Research*, 96(B10): 1642916454, 1991. doi: 10.1029/91JB00899.

Snoke, J. A. Traveltime tables for iasp91 and ak135. *Seismological Research Letters*, 80(2):260–262, 2009.

Tomlinson, E., Smith, V., and Menzies, M. Chemical zoning and open system processes in the Laacher See magmatic system. *ontributions to Mineralogy and Petrology*, 175(19), 2020. doi: https://doi.org/10.1007/s00410-020-1657-4.

Walker, K., Bokelmann, G., Klemperer, S., and Bock, G. Shear-wave splitting around the Eifel hotspot: evidence for a mantle upwelling. *Geophysical Journal International*, 163(3), 2005. doi: 10.1111/j.1365-246X.2005.02636.x.

Ward, K. and Lin, F. On the viability of using autonomous three-component nodal geophones to calculate teleseismic Ps re-

ceiver functions with an application to Old Faithful, Yellowstone. *Seismological Research Letters*, 88:1268–1278, 2017. doi: https://doi.org/10.1785/0220170051.

Yuan, X., Ni, J., Kind, R., Mechie, J., and Sandvol, E. Lithospheric and upper mantle structure of southern Tibet from a seismological passive source experiment. *Journal of Geophysical Research*, 102:27491–27500, 1997. doi: https://doi.org/10.1029/97JB02379.

Zhu, W. and Beroza, G. C. PhaseNet: a deep-neural-network-based seismic arrival-time picking method. *Geophysical Journal International*, 216(1):261–273, 10 2018. doi: 10.1093/gji/ggy423.